Robust half-metallicities of alkali-metal-based half-Heusler compounds

T. Thuy Hoang, S. H. Rhim,* and S. C. Hong†
Department of Physics and Energy Harvest Storage Research Center, University of Ulsan, Ulsan 44610, Republic of Korea

(Received 11 January 2022; revised 25 March 2022; accepted 19 April 2022; published 6 May 2022)

This paper aims to perform a systematic density functional study on alkali-metal-based half-Heusler compounds, namely ACrZ (A = Li, Na, and K; Z = As, Sb, and P), to identify the optimal half-metal (HM) for practical applications. Unlike most HMs proposed so far, the majority of ACrZ compounds in our study exhibit a wide band gap (1.60–2.38 eV) and retain robust half-metallicity even at the surface. Furthermore, the half-metallicity is robust under severe strain, up to 10%. Because of their stability, robust half-metallicity at the surface and under strain, and good lattice mismatch with zinc-blende semiconductors, we propose LiCrZ and NaCrZ (Z = As and Sb) as promising compounds for practical applications to spintronics.

DOI: 10.1103/PhysRevMaterials.6.055001

I. INTRODUCTION

Half-metals (HMs) are materials whose one spin channel behaves as a semiconductor and the other behaves as a metal [1,2]. The charge current in only one spin channel enhances the efficiency of spintronic devices, such as magnetic tunnel junctions [3,4]. Although HMs have been theoretically proposed in various materials, only a few have been confirmed experimentally [1]. Among the proposed HMs, Heusler compounds have attracted significant interest since their chemical composition can be altered for diverse functionalities [5,6]. Most of them also have high Curie temperature T_C [7]. There are two types of Heusler compounds, half-Heusler and full-Heusler, conventionally denoted as XYZ and X_2YZ, respectively. Herein, we focus on the half-Heusler compound XYZ and discuss its possible practical applications to spintronics.

The first theoretically predicted HM is the half-Heusler compound NiMnSb [2], with an estimated band gap of ~0.48 eV in the minority spin channel [2,8]. A few years later, the 100% spin polarization (SP) of NiMnSb was confirmed at a low temperature (10 K) [9]. However, its SP dropped significantly to nearly 50% at room temperature [10,11]. Subsequently, systematic density functional studies on XYZ have been performed intensively to find optimal HMs for practical applications [8,12], where X and Y are the transition elements and Z is an sp element. Even though some Co-based compounds are predicted to have wider band gaps than that of NiMnSb [8], most XYZ compounds have band gaps below 1 eV. HMs have also been predicted in certain X_2YZ compounds (X = Co, Fe, Rh, and Ru; Y = Ti, V, Cr, Mn, and Fe; Z = Al, Ga, In, Tl, Ge, Sn, and Pb) [13]. Although some Co-based compounds were successfully synthesized [14,15], they failed to achieve high SP at room temperature [16–18], except for Co_2MnSi [19]. The predicted narrow band gaps (0.2–0.5 eV) are the plausible origin of the failure [20].

The reduced SP has been attributed to thermal and surface/interface effects [1]. Thermal fluctuation may lead to spin depolarization at elevated temperatures [21–24]. At surfaces/interfaces, chemical composition and symmetry different from bulk may also decrease SP [25–28]. Above all, materials with wide band gaps likely retain half-metallicities even under high temperatures and at surfaces/interfaces [1,29]. Most studies are dedicated to transition-metal (T)-based Heusler compounds. However, due to their relatively narrow band gaps they lose half-metallicity easily. Meanwhile, alkali-metal(A)-based Heusler compounds have been relatively overlooked, despite some meaningful theoretical works [30–36] having been done previously. Hereafter, we differentiate the A-based from the T-based compounds by denoting them as AYZ and TYZ (or T_2YZ), respectively. LiMnSi is the first predicted AYZ to exhibit half-metallicity at a lattice constant expanded by 14% [30]. Subsequently, other AYZ, such as LiCrAs [31], NaCrAs [32], NaCrP [33], KMnP [34], and NaZrZ (Z = P, As, and Sb) [35], were predicted to be HMs. Broadly, AYZ tends to show much wider band gaps than TYZ. For example, the band gap of NaCrP is 3.21 eV [33], while that of CoCrP is 1.34 eV [8]. Furthermore, NaCrAs preserves its half-metallicity at the (001), (010), and (111) surfaces with hydrogen adsorption [32]. It is also notable that CsCrS, where a VI element is employed for Z instead of a V element of the present ACrZ, shows the wide band gap of 1.926 eV with the large magnetic moment of $5\mu_B$ [36].

Herein, we extend systematic density functional study on the half-metallicities of alkali-metal-based half-Heulser compounds, i.e., ACrZ (A = Li, Na, and K; Z = As, Sb, and P). Most investigated ACrZ show half-metallicities with wide band gaps (1.60–2.38 eV) at their equilibrium lattice constants. The band gaps originate from the sublattice zinc-blende (ZB) CrZ. An alkali-metal element serves to expand lattice constant, widens the band gap, and provides one more valence electron to the system. Further, the robustness of half-metallicity against strain and at surface/interface is analyzed to suggest optimal HMs for real applications. Moreover, formation energy is estimated and discussed for structural stability.

*sonny@ulsan.ac.kr
†schong@ulsan.ac.kr

 ©2022 American Physical Society

TABLE I. The possible phases of half-Heusler compound XYZ.[a]

Structure	X	Y	Z	Rocksalt	Zinc blende
α	$4c$	$4b$	$4a$	YZ	XY, XZ
β	$4b$	$4a$	$4c$	XY	YZ, XZ
γ	$4a$	$4c$	$4b$	XZ	XY, YZ

[a]The positions ($4a$, $4b$, and $4c$) are denoted in terms of the Wyckoff notation and the sublattice structures are presented.

II. STRUCTURAL MODELS AND COMPUTATIONAL METHODOLOGY

The half-Heusler and the regular full-Heusler compounds crystallize in the noncentrosymmetric cubic $C1_b$ structure with the $F\bar{4}3m$ (no. 216) space group and in the centrosymmetric cubic $L2_1$ structure with the $Fm\bar{3}m$ (no. 225) space group, respectively [37]. Regular X_2YZ and α-phase XYZ are based on the rocksalt (RS) sublattice of YZ. The additional X in regular X_2YZ (α-phase XYZ) occupy (every other) body center of the RS sublattice. Unlike the regular X_2YZ, in XYZ, XY, or XZ it also forms the RS sublattice. Three possible phases (α, β, and γ) of XYZ are listed in Table I. The most stable β phase is presented in Fig. 1(a) [30], where the element Z is positioned in every other body-centered site of the RS structure of ACr. From another viewpoint, the β phase is based on the ZB structure of CrZ into which fcc A fits.

Figure 1(b) represents an asymmetric slab of 14 layers exhibiting ACr termination (ACr-term) and Z termination (Z-term) to simulate two nonequivalent bulk terminations. Surface, subsurface, and center layer are denoted as (S), (S-1), and (C), respectively. The vacuum spacing of 15 Å between adjacent slabs eliminates any spurious interactions.

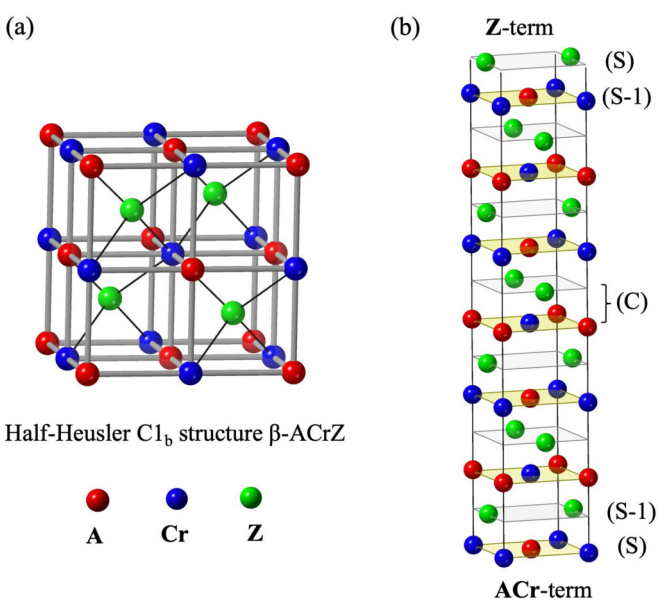

FIG. 1. (a) The C_{1b} structure of the β-phase half-Heusler ACrZ compound and (b) 14-ML slab to simulate ACr-term and Z-term ACrZ (001) surfaces. Red, blue, and green spheres represent A, Cr, and Z atoms, respectively. Surface, subsurface, and center layers are denoted by (S), (S-1), and (C), respectively.

The increased number of layers changes the physical properties negligibly, including magnetic moments ($<0.002\mu_B$) and interlayer distances (<0.003 Å), implying that the 14 layers are thick enough to simulate the ACr- and Z-term surfaces.

Density functional calculations are performed using Vienna Ab initio Simulation Package [38]. The generalized gradient approximation of the Perdew, Burke, and Ernzerhof [39] is used for the exchange-correlation interaction within the projector augmented-wave scheme [40]. An energy cutoff of 550 eV is used for the wave function expansion. For Brillouin zone integration, the k-point meshes of $15 \times 15 \times 15$ and $21 \times 21 \times 1$ in the Monkhorst-Pack scheme are employed for the bulk and surface calculations, respectively. Convergence for the number of k points is tested critically. In the surface calculations, interlayer distances are relaxed with the force criteria of 1×10^{-3} eV/Å.

III. RESULTS AND DISCUSSION

We first estimated the structural and magnetic phases of ACrZ from total energy calculations as functions of lattice constant. The results are presented in Figs. S1 and S2 of the Supplemental Material [41]. Table II summarizes the stable phase and energy difference between the antiferromagnetic (AFM) and ferromagnetic (FM) states ($\Delta E = E_{\mathrm{AFM}} - E_{\mathrm{FM}}$). The FM state is more stable than the AFM state over a wide range of lattice constants. Structurally, ACrZ in the β phase is most stable, except for KCrSb, which prefers the γ phase. Even though the FM stability of a K-based compound is insensitive to the atomic number, with an increasing atomic number of Z, the FM state tends to stabilize further than the AFM state (Table II). The estimated equilibrium lattice constants in the FM states of ACrP are 5.69, 6.15, and 6.75 Å, of ACrAs are 6.00, 6.37, and 6.94 Å, and of ACrSb are 6.42, 6.78, and 7.29 Å for A = Li, Na, and K, respectively. The larger atomic numbers of A and Z result in the larger lattice constant.

A. Magnetic property

The magnetic moments are listed in Table II. As expected, the magnetic moment of ACrZ corresponds mainly to the transition element Cr, while the contributions from other elements are negligible. Specifically, the magnetic moment of the alkali-metal element A is too small to be listed in Table II. The sp element Z has a negatively induced magnetic moment. Notably, unlike ACrZ with a small lattice constant, the one with a large lattice constant has an integer magnetic moment (in μ_B). Since the integer magnetic moment indicates half-metallicity, the lattice constant plays a crucial role in determining the half-metallicity of ACrZ, as discussed in the following subsections.

The Slater-Pauling rules can estimate the magnetic moment of HMs [37]. The Slater-Pauling rule for HM β-ACrZ is the so-called "rule of 8," expressed as $m_{\mathrm{tot}} = (Z_t - 8)\mu_B$, where Z_t is the total number of valence electrons. By this rule, the magnetic moment of HM β-ACrZ is estimated as $4.00\mu_B$, which is consistent with the observed first-principles calculations. We remind here that the magnetic moment of HM ZB-CrZ, a sublattice of β-ACrZ [Fig. 1(a)], is estimated as $3.00\mu_B$ by the same rule [42]. Thus, presumably, the alkali-

TABLE II. Energy difference ΔE (meV/f.u.) between AFM and FM states, equilibrium lattice constant a (Å), atom-projected magnetic moment (μ_B), total magnetic moment per formula unit (μ_B), band gap (eV) of minority spin state E_g, and k points of CBM and VBM of $ACrZ$. The asterisk (*) indicates pseudo band gap.

Compound	Phase	ΔE	a	m_{Cr}	m_Z	m_{tot}	E_g	CBM-VBM
LiCrP	β	27	5.69	3.35	−0.15	3.51	1.99*	X-Γ
NaCrP	β	161	6.15	3.82	−0.19	4.00	2.28	X-L
KCrP	β	184	6.75	3.97	−0.25	4.00	2.38	X-X
LiCrAs	β	142	6.00	3.62	−0.12	3.98	1.90*	X-Γ
NaCrAs	β	196	6.37	3.73	−0.18	4.00	2.18	X-L
KCrAs	β	187	6.94	3.88	−0.26	4.00	2.13	Γ-X
LiCrSb	β	231	6.42	3.67	−0.14	4.00	1.60	X-Γ
NaCrSb	β	222	6.78	3.79	−0.20	4.00	1.88	X-Γ
KCrSb	γ	187	7.29	3.90	−0.24	4.00	2.17	X-L

metal element A provides one more valence electron to the system to enhance the magnetic moment by $1\mu_B$.

B. Band gap

Figure 2 shows the band structures of $ACrZ$, indicating the half-metallicity character of $ACrZ$. Gray and black lines represent the majority and minority spin bands, respectively. The blue horizontal line indicates the Fermi level E_F set to zero. Red lines mark the conduction band minimum (CBM) and the valence band maximum (VBM) with an arrow suggesting the band gap width. The minority spin bands have gaps at E_F, except for LiCrP and LiCrAs, while the majority bands are metallic. In other words, $ACrZ$ are HMs, except for LiCrP and

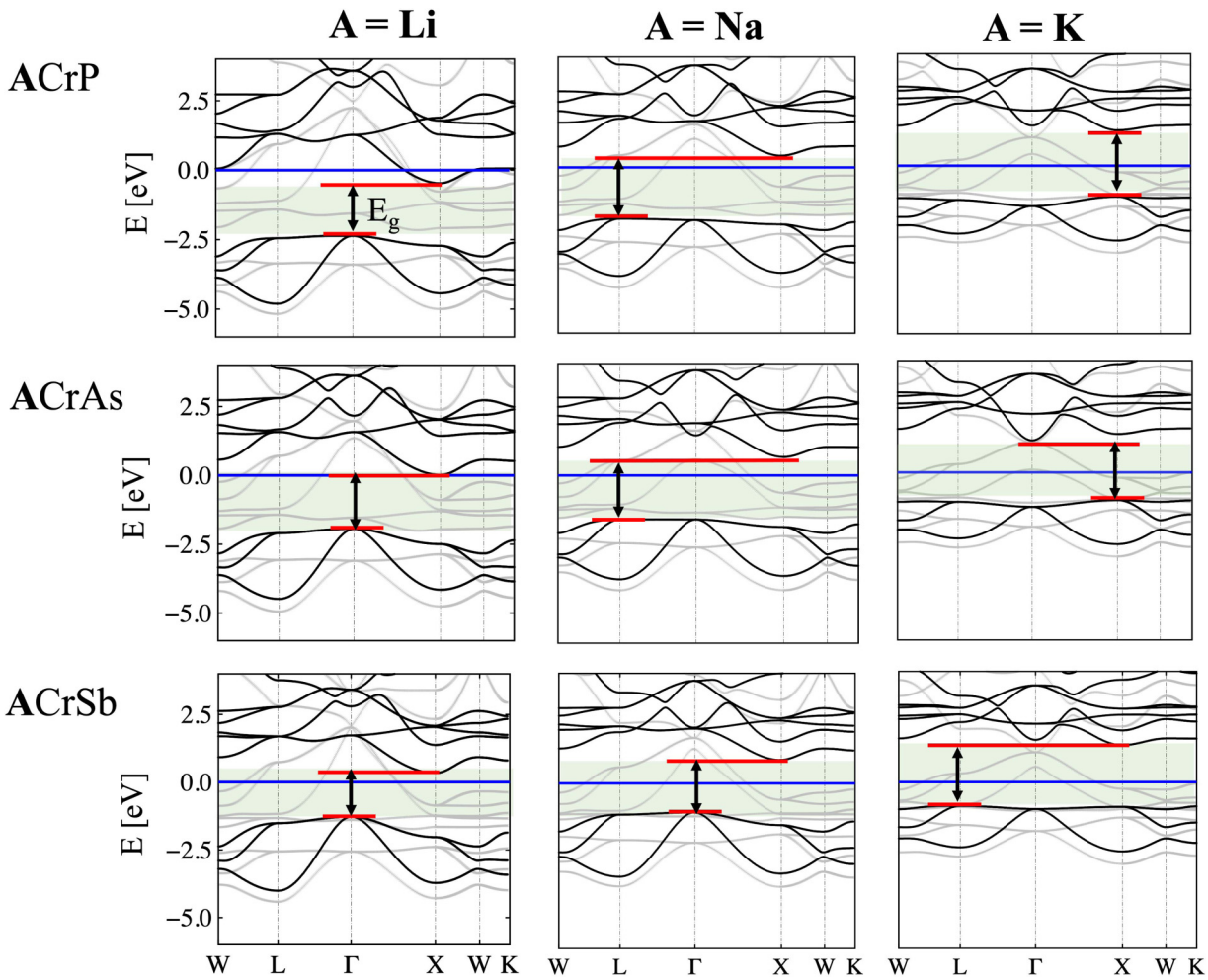

FIG. 2. Majority and minority spin band structures of $ACrZ$ (A = Li, Na, and K; Z = As, Sb, and P) at their equilibrium lattice constants. Red lines mark CBM and VBM.

LiCrAs. The estimated energy band gaps are listed in Table II. The asterisk on the value implies a pseudo band gap located at energy other than E_F. Table II shows that the HM compound has an integer magnetic moment (in μ_B).

The investigated ACrZ have much wider band gaps (1.60–2.38 eV) than previously reported HMs, including TYZ and T_2YZ; namely, NiMnSb (∼0.48 eV) [2,8], Co_2MnSi (0.41 eV) [14], Co_2MnGe (0.21 eV) [14], CrO_2 (1.50 eV) [43], and Fe_3O_4 (0.50 eV) [44]. Most of the band gaps are indirect; the CBM of ACrZ (except KCrAs) are located at the same k point X, while their VBM are located at different k points (Table II). Only KCrP has a direct band gap. Noteworthy, KCrSb almost has a direct band gap because of the negligible difference (∼0.03 eV) between the maxima at the X and L points in the valence band of KCrSb. The external factors, such as heat, surface, and interface, may break the half-metallicity with a narrow band gap, suggesting the wide band gaps of ACrZ must be advantageous in real applications [1,29].

C. Origin of wide band gap

Now we discuss the origin of the relatively wide band gaps of ACrZ other than those of the conventional TYZ. As listed in Table II, most ACrZ stabilizes in the β phase, unlike TCrZ, which stabilizes in the α phase [8]. This phase difference results in different band gap formation mechanisms, as discussed in detail below. ZB-TCr provides the band gap of TCrZ [45,46], while the band gap of ACrZ will be seen to originate from ZB-CrZ. Three key facts are established from Table II: (i) a large A atom corresponds to a wide band gap of ACrZ, (ii) a large Z atom indicates a narrow band gap, and (iii) only ACrZ with a lattice constant larger than 6.00 Å are HMs. Therefore, the lattice constant plays a key role in determining the half-metallicity of ACrZ. It is usually expected that a band gap formed between bonding and antibonding states is expected to narrow, as the lattice constant increases. For example, a TCrZ compound, RuCrAs ($a = 5.74$ Å, $E_g = 0.58$ eV) [8] has a considerably smaller band gap than FeCrAs ($a = 5.48$ Å, $E_g = 0.96$ eV) [8,46]. However, the band gap of the present ACrZ widens with the lattice constant expansion.

The origin of the wide band gap of ACrZ may be revealed by comparing their band structure with that of the sublattice ZB-CrZ [Fig. 1(a)]. ZB-CrZ itself is known to be an HM at or near its equilibrium lattice constant [47], which is evident from our calculations presented in Fig. S3 [41]. Here NaCrAs and CrAs are taken as representatives of ACrZ and ZB-CrZ, respectively. The orbital-resolved minority spin band structures of NaCrAs and ZB-CrAs are presented in Fig. 3 for comparison, employing the same lattice constant of equilibrium a for NaCrAs. The band structure of NaCrAs is similar to that of ZB-CrAs but the band gap is slightly narrowed. It shows clearly that the origin of the band gap formation of NaCrAs is identical to that of ZB-CrAs. The d orbitals of Cr are split into t_{2g} and e_g states in the tetrahedral environment, where Cr (As) is surrounded by four nearest neighbor As (Cr).

Hence, it may be enough for disclosing of the wide band gap of ACrZ to discuss the dependence of the band gap of CrAs on the lattice constant. According to the band gap formation of ZB-CrZ [42,47], the t_{2g} states of Cr form bonding and antibonding hybrid states with the p orbitals of As, while

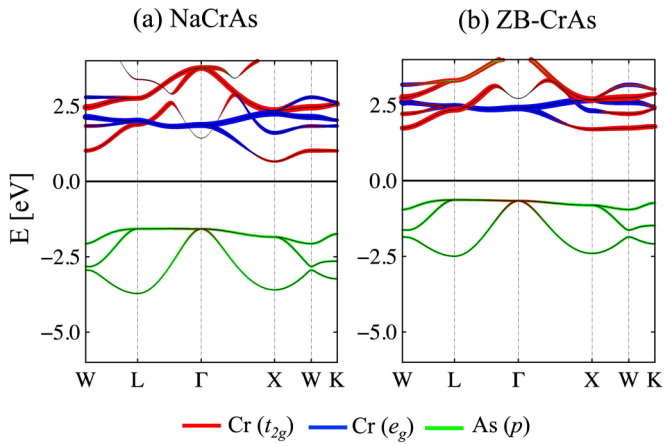

FIG. 3. Orbital-resolved minority spin band structure of NaCrAs and ZB-CrAs at equilibrium lattice constant of NaCrAs $a = 6.37$ Å. Cr-t_{2g}, Cr-e_g, and As-p orbitals are denoted in red, blue, and green, respectively. The symbol size is proportional to the weight of the orbital. The Fermi level E_F is set to zero.

the e_g states remain comparatively nonbonding. The band gap is formed by As-p orbital (bonding) and Cr-t_{2g} orbital (antibonding) states, as seen in Fig. 3. The band gap of ZB-CrAs increases monotonically with lattice constant a, as shown in Figs. S4–S6 of the Supplemental Material [41]. When a reaches 6.37 Å (equilibrium lattice constant of NaCrAs) from 5.66 Å, the band gap increases from 1.85 to 2.33 eV, which is slightly larger than the 2.18 eV of NaCrAs. Two factors compete in determining the width of the band gap. First, the covalent bonding weakens as the lattice expands, thus the band gap tends to reduce the width of the gap. Another effect of the lattice expansion is to narrow the valence and conduction bands themselves, which effectively widens the band gap, as shown in Fig. S6 [41]. To see the effects, the centers of the As-p VB and the Cr-t_{2g} and Cr-e_g CB are calculated from the orbital-decomposed DOS presented in Fig. S6 [41]. As expected, separation between the centers of VB and CB decreases as the lattice increases due to weakened covalent bonding, as listed in Table S1 [41]. However, separation between the edges of VB and CB increases because CB and VB narrow down as the lattice increases. The band gap widening by the narrowed bands is dominant over the band gap narrowing by the weakened covalent bonding in CrAs. Thus, the band gap of CrAs increases as the lattice constant increases. The element A in ACrZ expands the lattice constant and provides one extra valence electron, which fills the spin-up bands but negligibly affects the spin-down band. Consequently, the band gap is widened with increased magnetic moment by $1\mu_B$ compared to ZB-CrZ.

D. Formation energy

The structural stability estimated by formation energy is of crucial importance in practical applications. To investigate the structural stability, the formation energy of ACrZ against the decomposition into bcc A and ZB-CrZ is calculated using the following equation:

$$E_{\text{form}} = E_{A\text{CrZ}} - (E_A + E_{\text{CrZ}}), \quad (1)$$

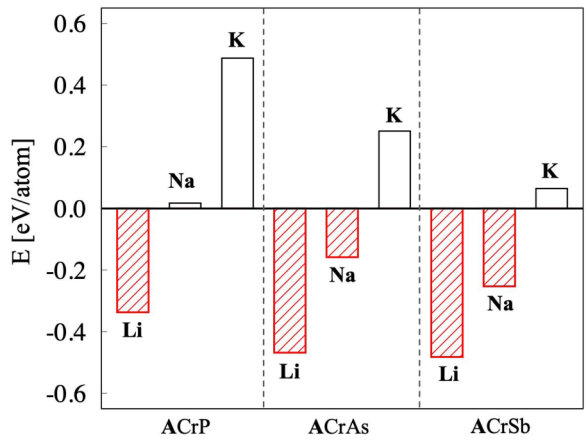

FIG. 4. Formation energies of ACrP, ACrAs, and ACrSb (A = Li, Na, and K). Left, middle, and right panel present ACrP, ACrAs, and ACrSb, respectively. Negative (positive) formation energy denotes a stable (unstable) structure.

where E_{ACrZ}, E_A, and E_{CrZ} are the total energies of ACrZ, bcc A, and ZB-CrZ, respectively. The formation energy is much more conservative against the decomposition into elements of A, Cr, and Z. The estimated formation energies of ACrP, ACrAs, and ACrSb (A = Li, Na, and K) are presented in Fig. 4, where the role of A and Z elements are evident. The negative (positive) formation energy means that ACrZ is energetically more stable (unstable) against the composition into bcc A and ZB-CrZ. From Fig. 4, it is learned that, first, the atomic number of A plays a key role in determining the formation energy. The smallest Li and the largest K led to negative and positive formation energies, respectively. Second, the larger Z element resulted in the more negative formation energy of ACrZ. Consequently, LiCrSb and KCrP show the most and the least stable against the decomposition into bcc A and ZB-CrZ, respectively.

E. Strain effects

In practical applications to spintronics, magnetic materials are usually exposed to thin-film under strain. Furthermore, strain is also utilized to tailor the electronic and magnetic properties of materials. Thus, investigating the in-plane strain effect on the half-metallicity of ACrZ is crucial. Energy variations in CBM (E_{CBM}) and VBM (E_{VBM}) against the strain are plotted in Fig. 5. The in-plane strain is given by $\eta = (a - a_0)/a_0$, where a_0 and a are equilibrium and strained ab plane lattice constants, respectively. The lattice constant c, shown in Fig. S7 [41] as c/a ratio, is optimized from total energy calculations. Figure 5 shows that the half-metallicity

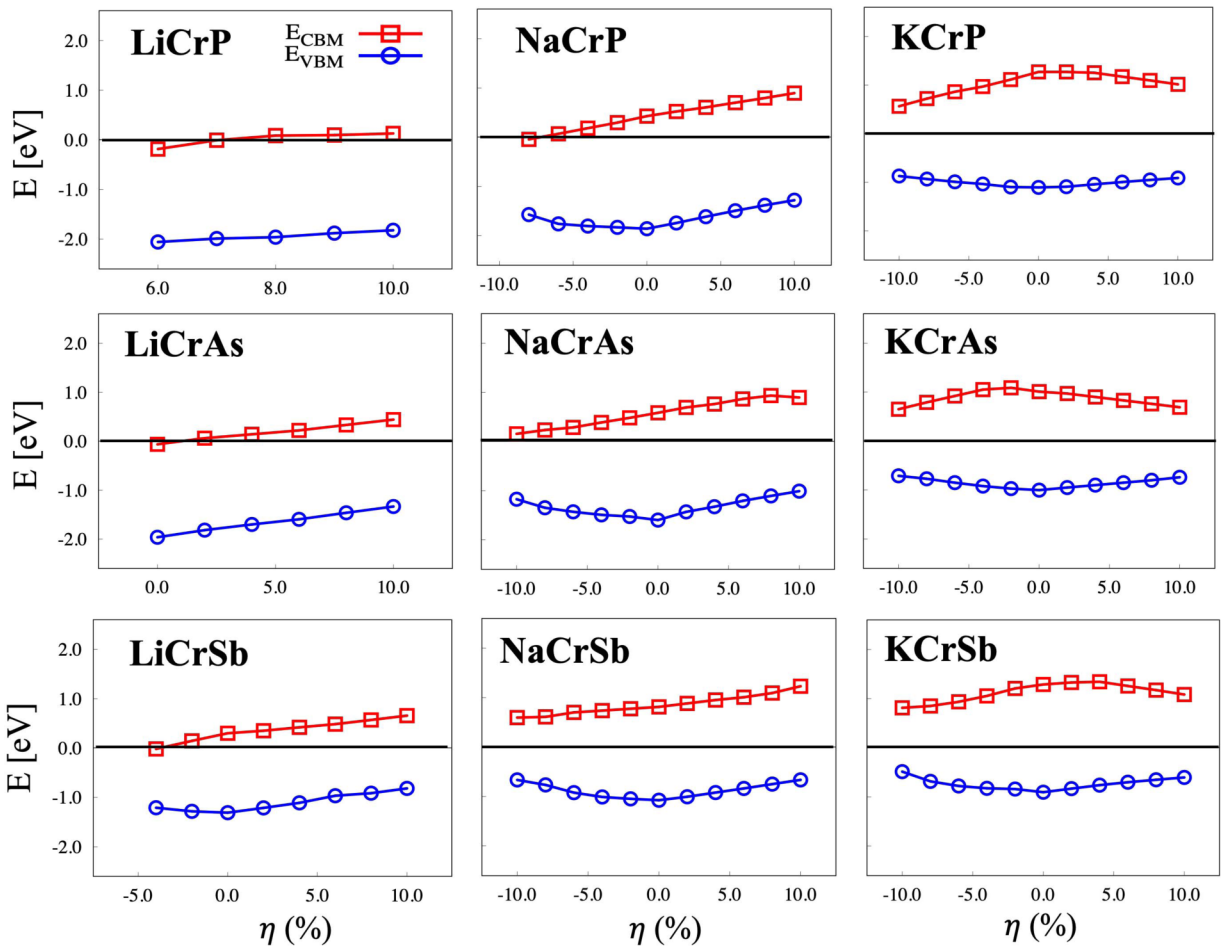

FIG. 5. E_{CBM} (in red) and E_{VBM} (in blue) of the minority spin states of ACrZ (A = Li, Na, and K; Z = As, Sb, and P) as a function of the in-plane strain. Fermi level E_F is set to be zero.

of unstrained $ACrZ$ is robust over a wide range of compressive and tensile strains, implying that HM $ACrZ$ has a flexible advantage in forming hybrid systems with various semiconductors. Even non-HM LiCrP and LiCrAs become HM under specific tensile in-plane strain. LiCrAs also turns into HM under small tensile strain, around +2%. Thus, the proper choice of substrate can easily achieve the half-metallicity of LiCrAs.

E_{CBM} and E_{VBM} under in-plane strain are discussed for practical device design. Figure 5 shows that E_{CBM} and E_{VBM} behave differently between the Li- and K-based compounds. The Na-based compounds show mixed behavior. First, E_{CBM} of the Li-based compounds (i.e., LiCrP, LiCrAs, and LiCrSb) is located just below or just above E_F at $\eta = 0$, while E_{VBM} is far below E_F. On the other hand, E_F of the K-based compounds (i.e., KCrP, KCrAs, and KCrSb) are positioned near the middle of E_{CBM} and E_{VBM}. Second, E_{CBM} and E_{VBM} of the Li-based compounds increase monotonically with η. As η increases, the E_{CBM} of LiCrP and LiCrAs shift above E_F from just below E_F, while the E_{CBM} initially far below E_F remain below E_F. Consequently, non-HM LiCrP and LiCrAs at their equilibrium turn to HM under specific tensile in-plane strain. Meanwhile, E_{CBM} and E_{VBM} behaviors of the K-based compounds are parabolalike with negative and positive curvatures, respectively. Interestingly, their E_{CBM} and E_{VBM} show maxima and minima near $\eta = 0$ to have the widest band gaps for the K-based compounds near unstrained states.

F. (001) surfaces

Practically, the magnetism and electronic structure at the surface/interface are more significant than in bulk. In real applications such as a magnetic tunnel junction, $ACrZ$ is likely utilized in a hybrid with a semiconductor [48,49]. We considered only the surfaces of LiCrAs, LiCrSb, NaCrAs, and NaCrSb to examine the magnetism and the half-metallicity at the (001) surface and excluded other $ACrZ$ due to their positive formation energies against the decomposition into bcc A and ZB-CrZ or non-half-metallicities.

1. Atomic structure

Reasonably, InSb is a potential semiconductor for a hybrid system with LiCrAs, LiCrSb, NaCrAs, and NaCrSb since the experimental lattice constant (6.48 Å) [50] of InSb exhibits rather good mismatches of +8.00%, +1.37%, +0.93%, and −4.42%, respectively. For surface calculations, the lattice constant of InSb is considered the in-plane lattice constant.

Two different terminations are plausible for the (001) surface: Z-term and ACr-term. As shown in Fig. 1(b), a 14-layer slab is used to simulate the Z- and ACr-term surface. The bulk properties shown by the center layers confirm the sufficient thickness of the slab. The interlayer spacings are fully relaxed by minimizing total energy and force. The relaxed structures are shown in Fig. S8 [41], and the numerical values of interlayer spacings and corrugations near the surfaces are presented in Table S2 [41]. The corrugation at ACr-term is more severe than at Z-term. The severe corrugation might be from the different valence electron characters of the Cr and A elements, i.e., d and s characters. The less localized A-s electron prefers spilling out into a vacuum to reduce its kinetic energy, while the relatively directional character of the Cr-d electron prefers staying inside to minimize energy at the expense of coming from a dangling bond.

TABLE III. Layer-resolved magnetic moment (in μ_B) of $ACrZ$ (A = Li, Na; Z = As, Sb) for (001) surface of both Z-term and ACr-term.[a]

		LiCrAs	NaCrAs	LiCrSb	NaCrSb
Z-term	Z(S)	−0.27	−0.37	−0.29	−0.38
	Cr(S-1)	3.12	3.31	3.09	3.28
Center	Z(C)	−0.14	−0.18	−0.13	−0.17
	Cr(C)	3.66	3.72	3.65	3.71
ACr-term	Cr(S)	3.92	3.99	4.06	3.97
	Z(S-1)	−0.09	−0.11	−0.08	−0.13

[a]Experimental lattice constant (6.48 Å) is employed for the two-dimensional lattice constant of the surface.

2. Magnetic moment

We present the magnetic moments of Cr and Z at the surface (S) and subsurface (S-1) layers in Table III, with the center layers (C) listed for comparison. Due to the reduced coordination number at the surfaces, the corresponding magnetic moments of the atoms are generally enhanced compared to those in the center layers. The magnetic moments of Cr(S) at the ACr-term surfaces of LiCrAs(Sb) and NaCrAs(Sb) increased by 7.10% (7.26%) and 11.23% (7.00%), respectively, and the magnetic moments of the subsurface Cr(S-1) atoms of the Z-term surfaces reduced by 14.75% (11.02%) and 15.30% (11.59%), respectively, compared to those of the center Cr layers. The magnetic moments of Z show a similar trend,

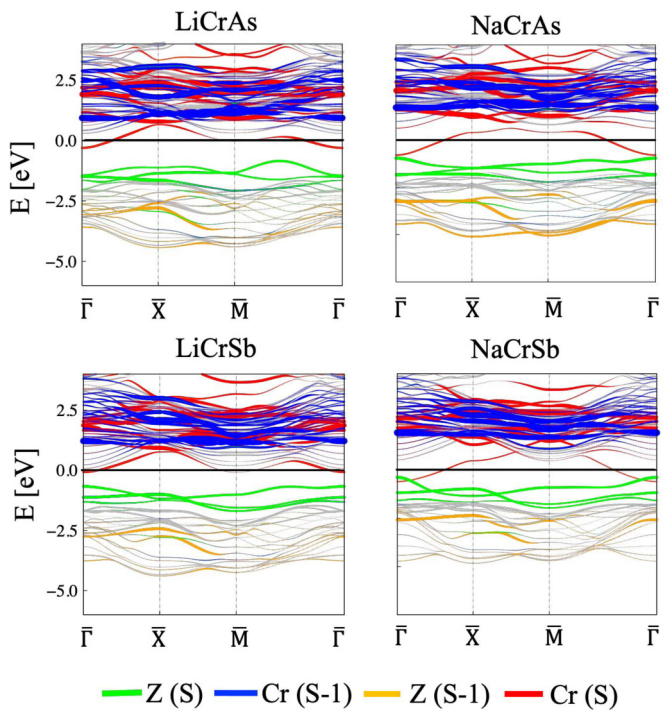

FIG. 6. Atom-resolved minority spin band structure of $ACrZ$ (A = Li and Na; Z = As and Sb) at Z-term and ACr-term (001) surfaces. The Fermi level E_F is set to zero.

TABLE IV. The band gaps (in eV) of $ACrZ$ (A = Li and Na; Z = As and Sb) of the Z-term (001) surface, the bulklike center layer, and the strained bulk.[a]

	LiCrAs	NaCrAs	LiCrSb	NaCrSb
Z-term	1.32	1.41	1.10	1.12
Center	1.82	2.10	1.58	1.76
Strained bulk	1.80	2.11	1.59	1.75

[a]The values of the strained bulk are estimated from Fig. 5.

enhanced, and reduced at the surfaces and the subsurfaces, respectively, compared to those of the center Z layers.

3. Half-metallicity

The left and right columns in Fig. 6 represent the two-dimensional minority spin bands of LiCrAs(Sb) and NaCrAs(Sb), respectively, to investigate the half-metallicity at the (001) surface. The bands originating from Z(S) and Cr(S-1) of Z-term are indicated in green and blue, and those from Cr(S) and Z(S-1) of ACr-term are shown in red and orange, respectively. Other bands are plotted in gray. Figure 6 demonstrates a robust half-metallicity at Z-term but a broken one at ACr-term. The severe corrugation at ACr-term shifts down the Cr(S) band crossing the Fermi level E_F. In practical devices, the $ACrZ$ compounds can be utilized an interfacial structure with various semiconductors. For example, at an interface $ACrZ$ with InSb, naturally InZ and CrSb bonding are expected to form at Z-term and ACr-term, respectively. In the interfacial structures, the bulklike half-metallicities would recover even for the broken half-metallicity at ACr-term.

Table IV lists the calculated band gaps at Z-term and the center layer. For comparison, the band gaps of the strained bulk LiCrAs (+8.00%), NaCrAs (+1.37%), LiCrSb (+0.93%), and NaCrSb (−4.42%) are also presented. The band gaps of Z-term LiCrAs, NaCrAs, LiCrSb, and NaCrSb are 1.32, 1.41, 1.10, and 1.12 eV, respectively, slightly smaller compared to the bulklike center layers (Table IV). The band gap values of the center layers are very close to that of the strained bulk ones. These findings reconfirm that the 14-layer slab is sufficiently thick to describe a bulk surface.

IV. CONCLUSION

Using first-principles calculations, we have studied the half-metallicity of alkali-metal-based half-Heusler, i.e., $ACrZ$ (A = Li, Na, and K; Z = P, As, and Sb), compounds. $ACrZ$, except for LiCrP and LiCrAs, are predicted to be HMs with wide band gaps in the range 1.60–2.16 eV, which would be advantageous for their practical applications. HM $ACrZ$ have an integer total magnetic moment $m_{\text{tot}} = 4.00\mu_B$, larger than the corresponding ZB-CrZ by $1\mu_B$, achieved from one more valence electron provided by the element A. Meanwhile, LiCrP and LiCrA showed magnetic moments below $4.00\mu_B$, which is 3.51 and $3.99\mu_B$, respectively, since their minority spin CBM is positioned just below the Fermi level E_F.

The band gap formation mechanism of $ACrZ$ is identified to be similar to that of ZB-CrZ, i.e., the hybridization between the Cr-d and Z-p states opens the band gap. The key role of the A element is twofold. The first is to expand the lattice constant, thereby widening band gaps, and the second is to achieve structural stability through formation energy. Furthermore, the half-metallicity is robust under severe in-plane strain and at Z-term. Overall, considering all the features discussed so far, including good lattice mismatch with ZB semiconductors, we propose LiCrZ and NaCrZ (Z = As and Sb) as promising compounds for real-life applications to spintronics.

ACKNOWLEDGMENT

This work was supported by National Research Foundation of Korea funded by Ministry of Science and ICT (Grants No. 2016M3D1A1027830 and No. NRF-2019R1I1A3A01059880).

[1] M. I. Katsnelson, V. Y. Irkhin, L. Chioncel, A. I. Lichtenstein, and R. A. de Groot, Half-metallic ferromagnets: From band structure to many-body effects, Rev. Mod. Phys. **80**, 315 (2008).

[2] R. A. de Groot, F. M. Mueller, P. G. van Engen, and K. H. J. Buschow, New Class of Materials: Half-metallic Ferromagnets, Phys. Rev. Lett. **50**, 2024 (1983).

[3] Y. Lu, X. W. Li, G. Q. Gong, G. Xiao, A. Gupta, P. Lecoeur, J. Z. Sun, Y. Y. Wang, and V. P. Dravid, Large magnetotunneling effect at low magnetic fields in micrometer-scale epitaxial $La_{0.67}Sr_{0.33}MnO_3$ tunnel junctions, Phys. Rev. B **54**, R8357 (1996).

[4] E. Y. Tsymbal, O. N. Mryasov, and P. R. LeClair, Spin-dependent tunnelling in magnetic tunnel junctions, J. Phys.: Condens. Matter **15**, R109 (2003).

[5] L. Wollmann, A. K. Nayak, S. S. Parkin, and C. Felser, Heusler 4.0: Tunable materials, Annu. Rev. Mater. Res **47**, 247 (2017).

[6] C. Felser, L. Wollmann, S. Chadov, G. H. Fecher, and S. S. P. Parkin, Basics and prospective of magnetic Heusler compounds, APL Mater. **3**, 041518 (2015).

[7] E. Şaşıoğlu, L. M. Sandratskii, P. Bruno, and I. Galanakis, Exchange interactions and temperature dependence of magnetization in half-metallic Heusler alloys, Phys. Rev. B **72**, 184415 (2005).

[8] J. Ma, V. I. Hegde, K. Munira, Y. Xie, S. Keshavarz, D. T. Mildebrath, C. Wolverton, A. W. Ghosh, and W. H. Butler, Computational investigation of half-Heusler compounds for spintronics applications, Phys. Rev. B **95**, 024411 (2017).

[9] K. E. H. M. Hanssen, P. E. Mijnarends, L. P. L. M. Rabou, and K. H. J. Buschow, Positron-annihilation study of the half-metallic ferromagnet NiMnSb: Experiment, Phys. Rev. B **42**, 1533 (1990).

[10] R. J. Soulen, J. M. Byers, M. S. Osofsky, B. Nadgorny, T. Ambrose, S. F. Cheng, P. R. Broussard, C. T. Tanaka, J. Nowak, J. S. Moodera, A. Barry, and J. M. D. Coey, Measuring the spin polarization of a metal with a superconducting point contact, Science **282**, 85 (1998).

[11] L. Ritchie, G. Xiao, Y. Ji, T. Y. Chen, C. L. Chien, M. Zhang, J. Chen, Z. Liu, G. Wu, and X. X. Zhang, Magnetic, structural,

and transport properties of the Heusler alloys Co_2MnSi and NiMnSb, Phys. Rev. B **68**, 104430 (2003).

[12] M. Baral and A. Chakrabarti, Half-metallicity versus symmetry in half-Heusler alloys based on Pt, Ni, and Co: An *ab initio* study, Phys. Rev. B **99**, 205136 (2019).

[13] I. Galanakis, P. H. Dederichs, and N. Papanikolaou, Slater-Pauling behavior and origin of the half-metallicity of the full-Heusler alloys, Phys. Rev. B **66**, 174429 (2002).

[14] P. Webster, Magnetic and chemical order in Heusler alloys containing cobalt and manganese, J. Phys. Chem. Solids **32**, 1221 (1971).

[15] M. Jourdan, E. A. Jorge, C. Herbort, M. Kallmayer, P. Klaer, and H.-J. Elmers, Interface and bulk magnetism of $Co_2Cr_{0.6}Fe_{0.4}Al$ and Co_2CrAl thin films, Appl. Phys. Lett. **95**, 172504 (2009).

[16] S. V. Karthik, A. Rajanikanth, Y. K. Takahashi, T. Okhubo, and K. Hono, Spin polarization of quaternary $Co_2Cr_{1-x}Fe_xAl$, Appl. Phys. Lett. **89**, 052505 (2006).

[17] A. Rajanikanth, D. Kande, Y. K. Takahashi, and K. Hono, High spin polarization in a two phase quaternary Heusler alloy $Co_2MnAl_{1-x}Sn_x$, J. Appl. Phys. **101**, 09J508 (2007).

[18] B. Varaprasad, A. Srinivasan, Y. Takahashi, M. Hayashi, A. Rajanikanth, and K. Hono, Spin polarization and Gilbert damping of $Co_2Fe(Ga_xGe_{1-x})$ Heusler alloy, Acta Mater. **60**, 6257 (2012).

[19] M. Jourdan, J. Minár, J. Braun, A. Kronenberg, S. Chadov, B. Balke, A. Gloskovskii, M. Kolbe, H. J. Elmers, G. Schönhense, H. Ebert, C. Felser, and M. Kläui, Direct observation of half-metallicity in the Heusler compound Co_2MnSi, Nat. Commun. **5**, 3974 (2014).

[20] S. Ishida, S. Fujii, S. Kashiwagi, and S. Asano, Search for half-metallic compounds in Co_2MnZ (Z = IIIb, IVb, Vb element), J. Phys. Soc. Jpn. **64**, 2152 (1995).

[21] L. Chioncel, E. Arrigoni, M. I. Katsnelson, and A. I. Lichtenstein, Electron Correlations and the Minority-Spin Band Gap in Half-Metallic Heusler Alloys, Phys. Rev. Lett. **96**, 137203 (2006).

[22] M. Ležaić, P. Mavropoulos, J. Enkovaara, G. Bihlmayer, and S. Blügel, Thermal Collapse of Spin Polarization in Half-Metallic Ferromagnets, Phys. Rev. Lett. **97**, 026404 (2006).

[23] B. Hu, K. Moges, Y. Honda, H. Liu, T. Uemura, M. Yamamoto, J. Inoue, and M. Shirai, Temperature dependence of spin-dependent tunneling conductance of magnetic tunnel junctions with half-metallic Co_2MnSi electrodes, Phys. Rev. B **94**, 094428 (2016).

[24] K. Nawa, I. Kurniawan, K. Masuda, Y. Miura, C. E. Patrick, and J. B. Staunton, Temperature-dependent spin polarization of Heusler Co2MnSi from the disordered local-moment approach: Effects of atomic disordering and nonstoichiometry, Phys. Rev. B **102**, 054424 (2020).

[25] G. A. de Wijs and R. A. de Groot, Towards 100% spin-polarized charge-injection: The half-metallic NiMnSb/CdS interface, Phys. Rev. B **64**, 020402(R) (2001).

[26] M. Ležaić, I. Galanakis, G. Bihlmayer, and S. Blügel, Structural and magnetic properties of the (001) and (111) surfaces of the half-metal NiMnSb, J. Phys.: Condens. Matter **17**, 3121 (2005).

[27] I. Galanakis, Surface properties of the half-and full-Heusler alloys, J. Phys.: Condens. Matter **14**, 6329 (2002).

[28] D. Steil, S. Alebrand, T. Roth, M. Krauß, T. Kubota, M. Oogane, Y. Ando, H. C. Schneider, M. Aeschli- mann, and M. Cinchetti, Band-structure-dependent Demagnetization in the Heusler Alloy $Co_2Mn_{1-x}Fe_xSi$, Phys. Rev. Lett. **105**, 217202 (2010).

[29] A. Mann, J. Walowski, M. Mu¨nzenberg, S. Maat, M. J. Carey, J. R. Childress, C. Mewes, D. Ebke, V. Drewello, G. Reiss, and A. Thomas, Insights Into Ultrafast Demagnetization in Pseudogap Half-Metals, Phys. Rev. X **2**, 041008 (2012).

[30] L. Damewood, B. Busemeyer, M. Shaughnessy, C. Y. Fong, L. H. Yang, and C. Felser, Stabilizing and increasing the magnetic moment of half-metals: The role of Li in half-Heusler LiMnZ (Z = N, P, Si), Phys. Rev. B **91**, 064409 (2015).

[31] R. L. Zhang, L. Damewood, Y. J. Zeng, H. Z. Xing, C. Y. Fong, L. H. Yang, R. W. Peng, and C. Felser, Two prospective Li-based half-Heusler alloys for spintronic applications based on structural stability and spin–orbit effect, J. Appl. Phys. **122**, 013901 (2017).

[32] M. Rostami, M. Abedi, P. Amantorkaman, and F. Kanjouri, DFT+U study of the bulk and (001), (110) and (111) surfaces of NaCrAs half-Heusler alloy with hydrogen adsorption for spintronics applications, Vacuum **175**, 109278 (2020).

[33] D. Hoat, M. Naseri, R. Ponce-Pérez, J. Rivas-Silva, A. Kartamyshev, and G. H. Cocoletzi, P-substitution effects on the electronic structure and thermal properties of the half-metallic half-Heusler NaCrBi compound, Chem. Phys **537**, 110848 (2020).

[34] A. Dehghan and S. Davatolhagh, d^0-d half-Heusler alloys: A potential class of advanced spintronic materials, J. Alloys Compd. **772**, 132 (2019).

[35] M. Moradi, N. Taheri, and M. Rostami, Structural, electronic, magnetic and vibrational properties of half-Heusler NaZrZ (Z = P, As, Sb) compounds, Phys. Lett. A **382**, 3004 (2018).

[36] Lin H. Yang, R. L. Zhang, Y. J. Zeng, and C. Y. Fong, *Design of Alkali-Metal-Based Half-Heusler Alloys Having Maximum Magnetic Moments from First Principles* (CRC, Boca Raton, 2018), pp. 69–77.

[37] T. Graf, C. Felser, and S. S. Parkin, Simple rules for the understanding of Heusler compounds, Prog. Solid State Chem. **39**, 1 (2011).

[38] G. Kresse and J. Furthmüller, Efficient iterative schemes for ab initio total-energy calculations using a plane-wave basis set, Phys. Rev. B **54**, 11169 (1996).

[39] J. P. Perdew and Y. Wang, Pair-distribution function and its coupling-constant average for the spin-polarized electron gas, Phys. Rev. B **45**, 13244 (1992).

[40] P. E. Blöchl, Projector augmented-wave method, Phys. Rev. B **50**, 17953 (1994).

[41] See Supplemental Material at http://link.aps.org/supplemental/10.1103/PhysRevMaterials.6.055001 for the structural and magnetic phases of *A*CrZ (*A* = Li, Na, and K; Z = P, As, and Sb), estimated from total energy calculations (Figs. S1 and S2); half-metallicity of ZB-CrZ (Z = P, As, and Sb) and band gap dependence of ZB-CrAs on lattice constant (Figs. S3-S6 and Table S1); the *c/a* ratio of tetragonal distortion due to in-plane strains as a function of in-plain strain η (%) of *A*CrZ (Fig. S7); and the relaxed structure, interlayer spacing d_{ij} and corrugation Δz_i at Z-term and *A*Cr-term (001) surfaces at an in-plane lattice constant of InSb (Fig. S8, Table S2), which is not shown in the main text.

[42] I. Galanakis and P. Mavropoulos, Zinc-blende compounds of transition elements with N, P, As, Sb, S, Se, and Te as half-metallic systems, Phys. Rev. B **67**, 104417 (2003).

[43] P. Schlottmann, Double-exchange mechanism for CrO_2, Phys. Rev. B **67**, 174419 (2003).

[44] H. T. Jeng and G. Y. Guo, First-principles investigations of the electronic structure and magnetocrystalline anisotropy in strained magnetite Fe_3O_4, Phys. Rev. B **65**, 094429 (2002).

[45] Z. Hao, R. Liu, Y. Fan, and L. Wang, First-principles calculations of a new half-metallic Heusler alloy FeCrAs, J. Alloys Compd. **820**, 153118 (2020).

[46] I. Galanakis, P. H. Dederichs, and N. Papanikolaou, Origin and properties of the gap in the half-ferromagnetic Heusler alloys, Phys. Rev. B **66**, 134428 (2002).

[47] J. E. Pask, L. H. Yang, C. Y. Fong, W. E. Pickett, and S. Dag, Six low-strain zinc-blende half metals: An ab initio investigation, Phys. Rev. B **67**, 224420 (2003).

[48] R. Farshchi and M. Ramsteiner, Heusler alloy/semiconductor hybrid structures, J. Appl. Phys. **113**, 191101 (2013).

[49] A. Hirohata, M. Kikuchi, N. Tezuka, K. Inomata, J. Claydon, Y. Xu, and G. van der Laan, Heusler alloy/semiconductor hybrid structures, Curr. Opin. Solid State Mater. Sci. **10**, 93 (2006).

[50] M. E. Straumanis and C. D. Kim, Thermal expansion coefficients, phase width, and perfection of the structure of GaSb and InSb, J. Appl. Phys. **36**, 3822 (1965).